ARTICLE

doi:10.1038/nature11649

The entorhinal grid map is discretized

Hanne Stensola[1]*, Tor Stensola[1]*, Trygve Solstad[1], Kristian Frøland[1], May-Britt Moser[1] & Edvard I. Moser[1]

The medial entorhinal cortex (MEC) is part of the brain's circuit for dynamic representation of self-location. The metric of this representation is provided by grid cells, cells with spatial firing fields that tile environments in a periodic hexagonal pattern. Limited anatomical sampling has obscured whether the grid system operates as a unified system or a conglomerate of independent modules. Here we show with recordings from up to 186 grid cells in individual rats that grid cells cluster into a small number of layer-spanning anatomically overlapping modules with distinct scale, orientation, asymmetry and theta-frequency modulation. These modules can respond independently to changes in the geometry of the environment. The discrete topography of the grid-map, and the apparent autonomy of the modules, differ from the graded topography of maps for continuous variables in several sensory systems, raising the possibility that the modularity of the grid map is a product of local self-organizing network dynamics.

A cardinal feature of mammalian neural organization is the topographic mapping of the external environment onto sensory areas of the neocortex. These sensory areas are further organized into layer-spanning spatial modules, or columns, consisting of cells that represent similar features of the sensory input[1–4]. In the somatosensory cortex, cells form columns that respond to specific somatic stimulus modalities[1]. In the visual cortex, cells may be organized into stripes or patches with similar eye dominance[2,3], orientation preference[4–7] or direction preference[8–11]. The topography of these and other sensory maps is thought to result from the formation of precise connections between sensory receptors and central target cells during early development[12–14].

Much less is known about functional circuit organization in higher-order non-sensory cortices. One of the few non-sensory systems with sufficiently distinct behavioural correlates to investigate structure–function relationships is the hippocampal–entorhinal space circuit. Many neurons in this circuit have known spatial firing correlates. 'Place cells' in the hippocampus fire only when animals visit certain locations[15–17]. These cells are probably generated, in part, from grid cells in the MEC, one synapse upstream[17–22]. Grid cells have multiple periodic firing fields, arranged for each cell in a hexagonal lattice that provides the network with a metric that place cells do not have on their own[17,19,21]. In both the hippocampus and the MEC, different cells fire at different locations[16,19], such that, collectively, the cells form neural maps of all locations in local space[16–18]. These maps are different from sensory maps in that spatial firing fields are not derived by extraction of features from a particular sensory input, but probably originate from pattern-formation processes in the circuit itself[17,21–28]. The mechanisms for topographical organization may thus be very dissimilar from those of the columnar sensory cortices.

The functional organization of the network that generates the grid pattern is not yet understood. We know that the grid map is distributed and topographical at the same time. The phase of the grid has a distributed representation in that firing fields of neighbouring grid cells do not overlap more than those of distant grid cells[19]. In contrast, grid scale is mapped topographically, in the sense that co-localized grid cells have similar grid spacing and grid spacing increases progressively from dorsal to ventral MEC[18–20]. However, because of limited sampling across MEC of individual animals, it has not been possible, despite theoretical suggestions[21,23] and experimental indications[29,30], to determine whether the gradient in grid spacing is continuous or modular and whether it is accompanied by changes in other properties of the grid. To establish whether the grid map is organized into discrete autonomous units, similar to those of some sensory cortices, and to reveal the organization and functional properties of any such modules, we recorded sequentially or simultaneously from 968 widespread grid cells in 15 animals, with up to 186 grid cells per animal.

We used two strategies (Fig. 1a). Five rats were implanted with a single bundle of 4 adjacent tetrodes angled tangentially to the MEC surface to allow grid cells to be recorded sequentially along a continuous dorsoventral strip of the superficial cell layers. Ten rats were implanted with a 1.0 mm × 1.25 mm oval array of 12 independently movable tetrodes, enabling parallel recording from grid cells across large parts of the MEC. Neural activity was sampled while the rats foraged in 100–220-cm-wide square boxes.

Grid scale has a discrete organization

We first investigated whether the progression in grid scale along the entorhinal dorsoventral axis is discrete or continuous. In rats with tangential tetrode implants, the recording tracks covered up to 1,800 μm of layers II and III, or more than one-third of the dorsoventral length of the MEC in the sagittal plane (1333 ± 349 μm, mean ± s.d., Supplementary Fig. 1). Within this range, we recorded up to 62 grid cells per animal (45.6 ± 19.0, mean ± s.d.). Grid spacing spanned from 35.2 cm to 171.7 cm (74.4 ± 35.6 cm, mean range ± s.d.). There was a strong positive correlation between grid spacing and tetrode depth across animals (Spearman rank correlation: $\rho = 0.34$, $P < 0.001$, $n = 228$ grid cells)[18–20] and within animals (mean $\rho \pm$ s.e.m.: 0.48 ± 0.09) (Fig. 1b).

The large number of grid cells obtained with the tangential tetrode tracks made it possible to determine, in individual animals, whether grid scale increases gradually or in discrete steps along the dorsoventral axis. The data pointed to a discrete organization in every single animal (Figs 1 and 2 and Supplementary Figs 1 and 2). Within animals, grid spacing clustered at distinct values, often with considerable gaps between successive clusters (Fig. 1d). To quantify the discreteness of the scale distribution, we counted the number of grid cells within successive bins of grid spacing, using a range of bin widths. Then,

[1]Kavli Institute for Systems Neuroscience and Centre for the Biology of Memory, Norwegian University of Science and Technology, Olav Kyrres gate 9, MTFS, 7491 Trondheim, Norway.
*These authors contributed equally to this work.

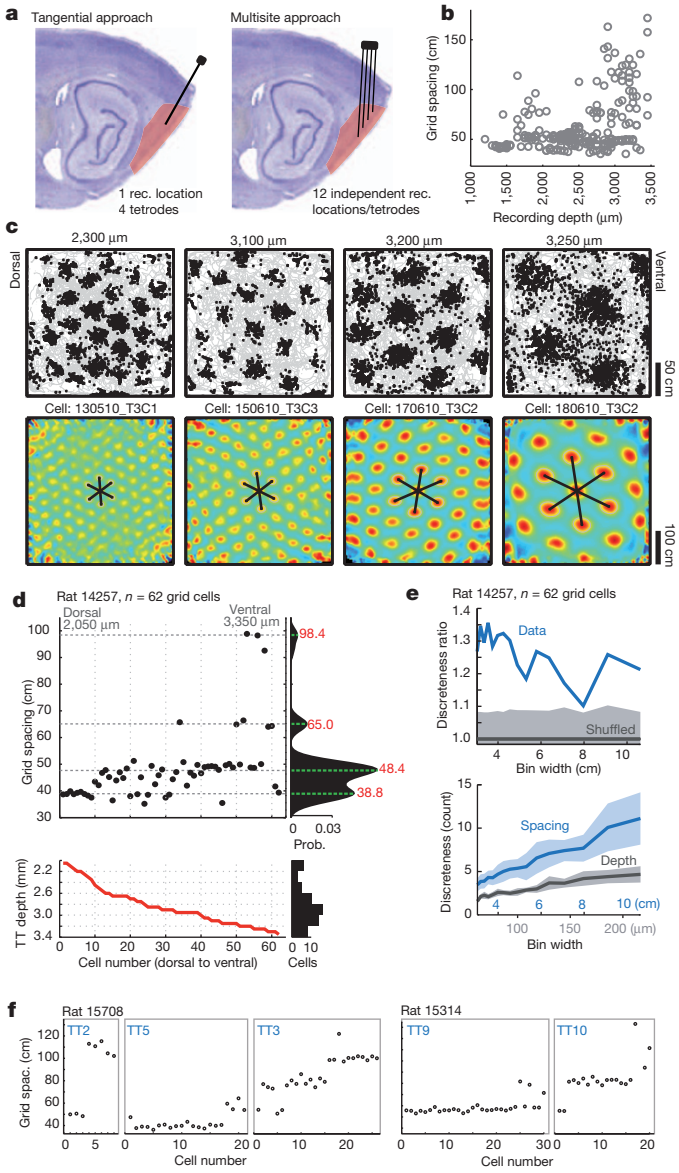

Figure 1 | Step-like increases in grid scale along the entorhinal dorsoventral axis. **a**, Schematic representation of tangential and multisite recording approaches (Nissl-stained sagittal sections, MEC highlighted in red). **b**, Scatterplot showing grid spacing as a function of dorsoventral recording position (all grid cells of all 'tangential' animals; increased recording depth corresponds to a more ventral location). **c**, Example grids at successive dorsoventral positions in a representative 'tangential' animal (rat 14257). Dorsoventral location from brain surface is indicated. Top, neuronal spikes (extracellular action potentials) overlaid on trajectory of rat (grey). Bottom, corresponding colour-coded autocorrelograms with colour scale (−1,1; blue is correlation of −1, red is correlation of 1). Grid spacing was determined from the innermost polygon (black axes). The spatial autocorrelogram reveals repeating activity patterns in the spatial rate map and is generated by correlating the rate map with itself at all spatial offsets. **d**, Grid spacing at successive dorsoventral levels in a single rat (TT, tetrode). Dots correspond to individual cells. Cells are plotted sequentially to avoid overlap between cells at similar depths. Right, kernel smoothed density (KSD) estimate of the distribution. Red text, spacing in cm for the estimated peaks. **e**, Top, the discreteness of the frequency distribution was calculated across multiple bin widths (Supplementary Fig. 3). Blue line, ratio of discreteness in recorded data and shuffled data in rat 14257. Light grey area, s.d. of shuffled data (mean 1.0, dark grey line). Bottom, discreteness of grid spacing compared to discreteness of recording depth for the same cells. Shadowed areas show s.d. of bin-count difference from mean. **f**, Grid scale of successively recorded cells at increasing dorsoventral depth on different tetrodes with the multisite approach. Tetrode numbering is arbitrary.

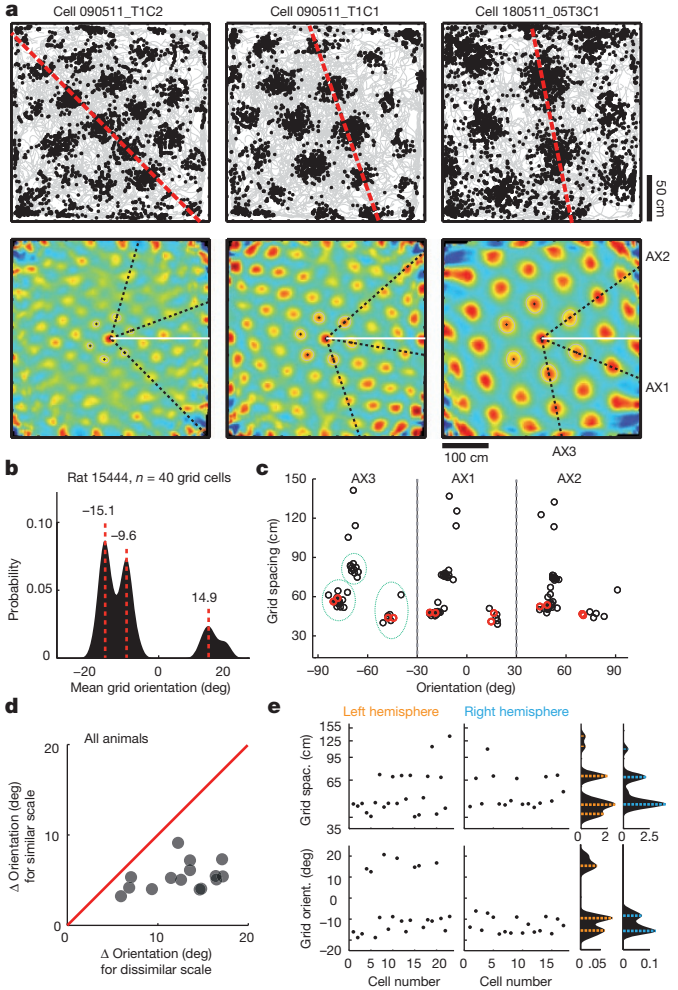

Figure 2 | Comodular organization of grid orientation and grid scale. **a**, Distinct grid orientations within one animal (rat 15444). Spike and autocorrelation maps as in Fig. 1c. Dashed lines indicate grid axes (AX). The white line is the horizontal reference (0 deg). Cells T1C1 and T1C2 were recorded simultaneously. **b**, KSD estimate of grid orientation in all cells from rat 15444 reveals three clear peaks (red dashed lines, peak grid orientations indicated). **c**, Grid spacing against grid orientation for all three grid axes in rat 15444. Each circle within each axis is one cell. Cells in red are from the same recording session. Note comodularity of orientation and spacing (green dashed outlines). **d**, Comparison of average orientation differences for pairs of grid cells with similar grid spacing (<5th percentile of scale differences) and pairs with different grid spacing (>5th percentile) in all 15 animals (one circle per data set). **e**, Left, scatter plots showing successively recorded values for grid spacing (top) and grid orientation (bottom) in separate hemispheres. Corresponding KSD estimates shown on right.

for each bin width, we calculated the standard deviation of differences in cell counts between bins and referred to this standard deviation as the discreteness of the distribution (Supplementary Fig. 3 and Supplementary Methods). Across all animals with more than 15 cells and a grid-spacing range of more than 20 cm, the discreteness was consistently larger for the observed data than for shuffled distributions of the same data (3.06 ± 0.58; mean $Z \pm$ s.e.m.; Fig. 1e, top). The mean discreteness for the distribution of recording depth was significantly lower than the mean discreteness for grid spacing in the same cell sample (Fig. 1e, bottom; discreteness ratio (spacing/depth) across bin widths, $P < 0.001$ in all animals). Collectively, these findings indicate that the distribution of grid spacing is discontinuous and that discontinuity is not caused by uneven cell sampling.

The discreteness of the scale gradient in animals with tangential tetrode tracks was reinforced by data from animals with semi-vertical

tetrode tracks at several locations. With the multisite approach, we recorded grid cells at distances up to approximately 1,000 μm apart along the mediolateral axis and 2,000 μm along the dorsoventral axis (Supplementary Fig. 4). These recordings produced high yields of grid cells (up to 186 cells in individual animals; 61.7 ± 67.0 cells, mean ± s.d.). The dorsoventral span of these recordings was sufficient to reveal steps in grid scale that mirrored those observed with the tangential approach (Fig. 1f and Supplementary Figs 2d–f and 4).

Grid orientation is discretized

We next asked whether other properties of the grid map follow a similar modular organization and whether the boundaries for any such modules are the same as for grid scale. We began by addressing the organization of grid orientation. Early studies of grid cells showed that co-localized cells express largely the same grid orientation[19], but the anatomically restricted sampling area of those studies precluded conclusions about whether all grid cells express the same orientation, or whether cells with different orientations exist in the same network. The widespread distribution of recording locations in the present study allowed us to address this question.

Two key observations were made. First, multiple discrete grid orientations were observed within animals and within recording sessions (Fig. 2a–c and Supplementary Figs 1 and 5). Second, the boundaries between these orientation modules coincided with boundaries between scale modules. Cells that belonged to the same scale module had similar grid orientations, whereas members of different scale modules often differed also in orientation (Fig. 2b, c and Supplementary Figs 5b and 6). In all 15 animals, grid orientation was more similar for cell pairs with similar grid scale (<5th percentile of all pairwise differences in grid scale) than for pairs with different scale (>5th percentile) (Fig. 2d and Supplementary Figs 6 and 7; mean ratio of orientation differences for pairs with different compared with similar scale: 2.73 ± 0.36, mean ± s.e.m., $t(15) = 8.37$ $P < 0.001$, 16 data sets, Student's t-test). In an animal with bihemispheric implants, mean values for grid scale and grid orientation were almost identical for left and right cluster pairs (Fig. 2e and Supplementary Fig. 1; mean peak differences ± s.e.m. of 1.4 ± 1.0 cm for scale and 0.6 ± 0.5 degrees for orientation).

Modular distortions of the grid pattern

Grid patterns can be distorted by changes in the shape of the environment. When a square test box is changed to a rectangle, the grid pattern may rescale selectively along the axis of transformation[30,31]. Similar asymmetries were observed in the present data, without preceding changes in the geometry of the environment (Fig. 3a and Supplementary Fig. 8). In many recordings, grid fields of co-localized neurons were consistently elongated in one direction (Fig. 3a, b). We asked whether these distortions were coherent across cells, and if they were not, whether differences followed the boundaries of modules for grid spacing and grid orientation. To quantify the distortions, we fitted ellipses to the six field centres of the inner polygon of the spatial autocorrelogram (Fig. 3a, b). From these ellipses, we determined ellipse tilt direction, ellipticity and eccentricity (see Supplementary Methods).

Grid cells with different distortion patterns could be observed within individual animals. Boundaries between cell clusters with different tilt directions coincided with boundaries between scale and orientation modules (Fig. 3a–d and Supplementary Fig. 9). In all 15 animals (16 data sets), the degree of grid distortion (Supplementary Fig. 8d and Supplementary Methods) was more similar for cell pairs with similar grid scale (<5th percentile of all pairwise differences in grid scale) than for pairs with different scale (>5th percentile) (Fig. 3d, ratio of grid distortion in cell pairs with different compared with similar scale: 3.17 ± 0.30, mean ± s.e.m., $t(15) = 10.33$, $P < 0.001$, Student's t-test).

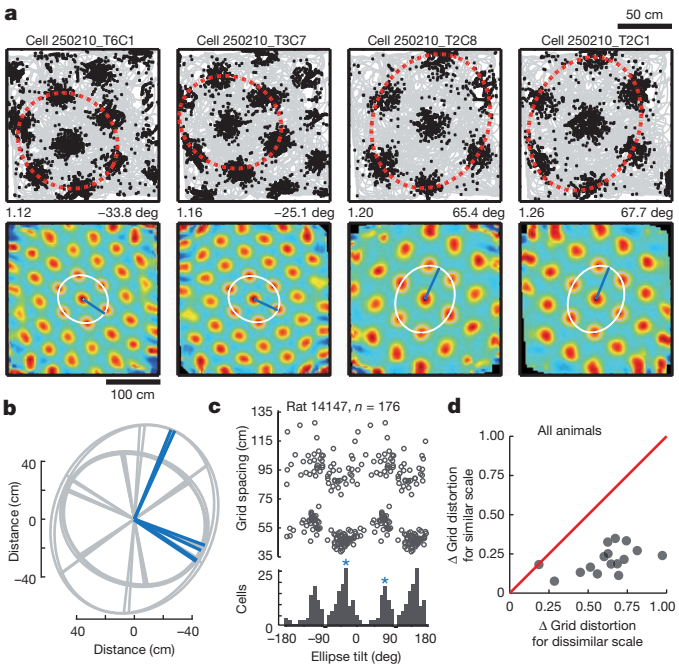

Figure 3 | Distortions in grid shape are comodular with grid spacing. **a**, Bimodal grid asymmetry within a single recording session (3 tetrodes, rat 14147). Maps as in Fig. 1c. Ellipses (white) were fitted to the inner polygon of the autocorrelogram. Corresponding ellipses on spike maps are shown in red. Blue lines and text on the upper right: ellipse-tilt (direction of semi-major axis). Text on the upper right: ellipticity. **b**, Ellipses calculated for all grids recorded in **a** ($n = 6$, 4 recording locations). **c**, Ellipse tilt as a function of grid scale (scatter plot and frequency distribution). Note the orthogonal bimodality (blue asterisks). Ellipse tilt ranged from −90 to 90 degrees, shown here from −180 to 180 for clarity. **d**, Comparison of average differences in grid eccentricity for pairs of grid cells with similar grid spacing (<5th percentile of scale differences) and pairs with different spacing (>5th percentile) in all 15 animals (methods as in Fig. 2d).

In animals with a bimodal distribution of ellipse tilt, the orientations were always close to orthogonal (Fig. 3b, c and Supplementary Fig. 8), indicating that the distortions were determined by the square shape of the recording environment. When an animal with a bimodal distribution was exposed to a circular environment, the distribution became unimodal, without any loss of ellipticity (Supplementary Fig. 10). The results indicate that asymmetries are coherent for grid cells within the same module, but may differ between modules depending on the environment.

Anatomical organization of grid modules

We next asked how modules with distinct grid scale, grid orientation and grid distortions are organized in anatomical space. We used a k-means algorithm based on grid scale, grid orientation and grid eccentricity to establish for the entire cell sample, with minimal experimenter bias, which cells belonged to which grid module (Supplementary Fig. 11 and Supplementary Methods). The k-value for each animal was determined from the number of local maxima detected in a two-dimensional kernel-smoothed-density estimate of distributions of grid scale and grid orientation (Supplementary Figs 11a and 12). The maximum k value was 5 (rat 14147).

First, in the tangential experiments, we noticed that the dorsoventral locations of the k-means-identified grid modules exhibited considerable overlap (Fig. 4a, b). The proportion of recording locations containing cells from more than one grid module was 37.0 ± 7.3%. A total of 10.3 ± 3.8% locations had more than two modules. The number of simultaneously recorded modules increased from dorsal to ventral MEC (mean correlation between dorsoventral location and s.d. of grid scale ± s.e.m., 0.68 ± 0.11, $P < 0.005$). The same sets of grid modules were identified in layers II and III (Supplementary

Fig. 13). Taken together these data indicate that grid modules are extensive and interspersed and cut across cortical layers.

One limitation of the tangential approach is that cells were sampled along a single track. To estimate the anatomical extent of the grid-cell modules, we turned to the multisite implants, which yielded from 2 to 10 grid-cell recording tracks in each animal (4.8 ± 2.8, mean ± s.d., predominantly MEC layers II and III, Supplementary Fig. 4). Surprisingly, the addition of recording tracks did not increase the number of *k*-means-identified grid modules (Fig. 4c, d). The dispersion of recording locations was determined by plotting them onto entorhinal flat maps in which the MEC is unfolded onto a two-dimensional surface (Fig. 4f). In animals with grid-cell recording locations spread apart as much as 900 μm along the mediolateral axis at a single dorsoventral level, only one cluster was identified (Supplementary Fig. 14). In animals with more extensive dorsoventral sampling and more than one grid module, values for grid scale and grid orientation were similar at widely separated mediolateral locations (Fig. 4e, f and Supplementary Figs 15 and 16), irrespective of cell layer (Supplementary Figs 4 and 13–15), indicating that, within the recording area in medial MEC, the modules may be organized as horizontal bands parallel to the dorsal border of the MEC. The maximum number of modules detected in any animal was four or five, with some uncertainty about the fifth module because the putative grids were too large for periodicity to be detected in this study (Supplementary Fig. 17). The largest area covered by tetrodes in any animal spanned nearly 50% of the dorsoventral axis and 32% of the mediolateral axis of MEC (Fig. 4e and Supplementary Fig. 14b), implying that the number of grid modules within MEC is small and, by extrapolation, in the upper single-digit range.

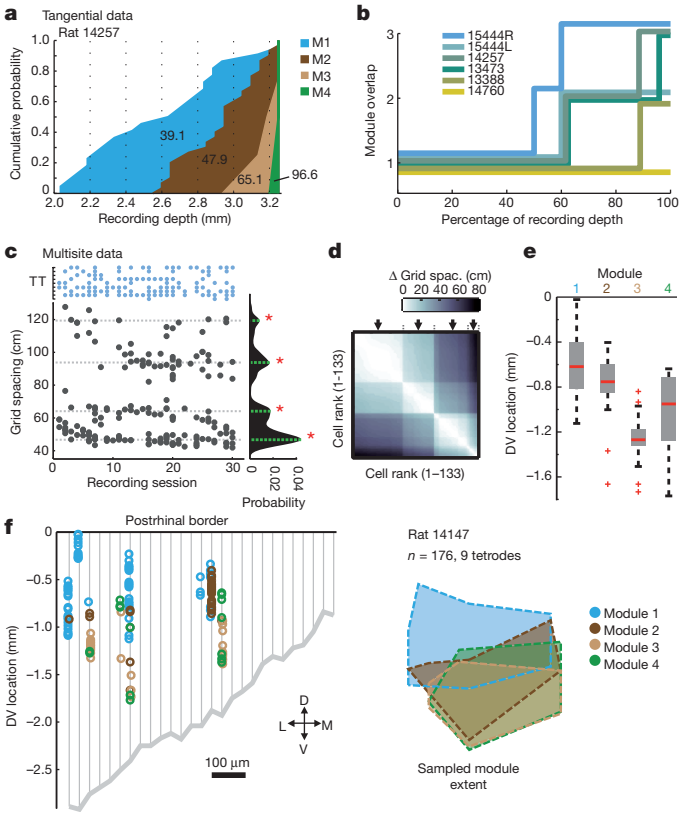

Figure 4 | Grid modules are organized as overlapping horizontal bands. **a**, Cumulative distribution of grid modules as a function of dorsoventral position in rat 14257 (62 grid cells, *k*-means-determined modules are colour-coded). Mean grid spacings in cm are indicated. **b**, Proportion of recording sites that had grid cells assigned to 1, more than 1, or more than 2 grid modules (all 'tangential' animals; L, left hemisphere; R, right hemisphere). **c**, Grid spacing for all grid cells in rat 14147. The same four grid modules were detected at other recording sites (KSD estimate and green lines/red asterisks on right). See Supplementary Fig. 17 for a possible fifth module. Top, tetrodes with grid cells on successive recording sessions. Each row corresponds to one tetrode; dots indicate sessions with grid cells. **d**, Similarity matrix showing differences in grid spacing for all grid-cell pairs in rat 14147 (133 grid cells from 20 sessions after experience-dependent stabilization[30]). Cells are ranked with respect to spacing (top and left, lowest value). Differences are coded by brightness (scale bar). Four blocks of grid spacing appear as abrupt transitions along the diagonal (black arrows). **e**, Boxplot showing dorsoventral (DV) distribution of recording locations for each module. Red lines, individual medians; grey boxes, 25th–75th percentile range; whiskers extend to extreme data points that are not considered outliers; red crosses, individual outlier data points ($n = 176$ in this plot). **f**, Left, flat map of the medial half of the MEC showing grid cell-containing recording positions in the same animal as in **c**. The *x* axis shows mediolateral position, *y* axis shows dorsoventral distance from the dorsal MEC border. Circles indicate recording locations for individual grid cells. Colour indicates module identity. Grid cells were recorded over approximately 50% of the dorsoventral axis and 20% of the mediolateral extent of the MEC (~1,900 μm and ~500 μm, respectively). Right, outline of each module (extrapolated from flat map, same scale).

Scale relations across modules

We asked whether module averages for grid spacing vary across animals and if there is a fixed scale relationship within animals. Mean grid-spacing values were widely distributed between rats, with no apparent peaks in the distribution (Fig. 5a, b and Supplementary Fig. 18). A significant scale relationship was revealed, however, when increases in grid spacing were plotted across animals as a function of module number, with modules ranked according to their mean grid spacing. Increments in grid spacing increased linearly between successive pairs of modules (from M2–M1 through M3–M2 to M4–M3) (Fig. 5c, $R^2 = 0.20$, $P = 0.027$). The ratio between successive module averages (M2/M1, M3/M2, M4/M3) fluctuated around a constant value of 1.42 (s.d. = 0.02; Fig. 5d), indicating that grid scale follows

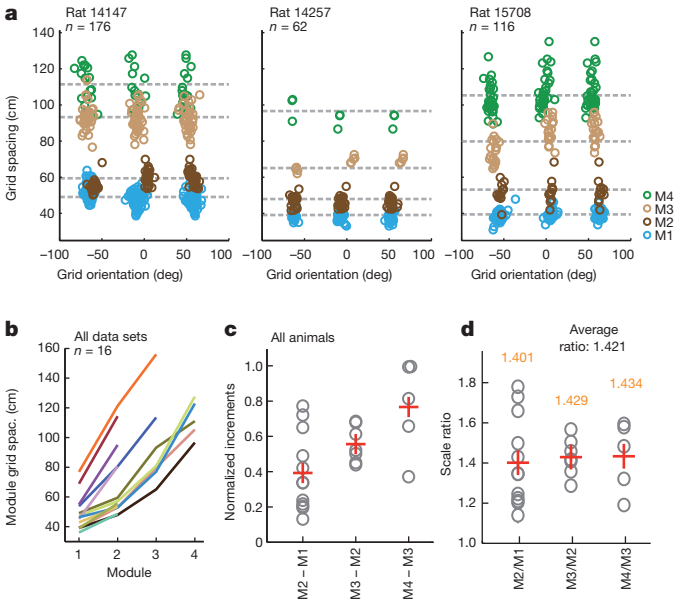

Figure 5 | Scale relationship between grid modules. **a**, Scatterplots showing difference in module grid-scale relationship for 3 animals, each with 4 detected modules (circles correspond to individual cells, modules are colour-coded). Spacing and orientation for all three axes are shown. Dashed lines, mean spacing of each module. **b**, Mean grid spacing for all modules (M1–M4) in all animals (animals colour-coded). Note variable module means and scale relationships across animals. **c**, Normalized increments in grid spacing (mean per module) as a function of module pair (M2 − M1: difference in mean grid spacing between module with lowest and second-lowest value, etc.). Individual module pairs are in grey, means across animals are in red. **d**, Ratios between successive module means for grid spacing. Individual module pairs in grey, means indicated by red crosses (values in orange).

a geometric progression rule. Note that a progression of approximately 1.42 ($\sqrt{2}$) translates to a near-perfect doubling of the area of the grid hexagon between modules of successive grid scale.

Grid modules have a discrete temporal organization

When MEC neurons fire in grid patterns, the local network activity is dominated by the theta rhythm[32,33]. To establish whether the organization of this rhythm is modular, we estimated the intrinsic theta frequency (ITF) of each cell in all eight animals with more than 35 grid cells in 2 or more modules. ITF was defined as the peak frequency in the theta band of the cell's spike-time autocorrelogram (Fig. 6). ITF was not uniformly distributed in MEC. When data were pooled across animals, there was a weak but significant negative correlation between ITF and grid spacing ($r = -0.12$, $P < 0.001$), as reported previously[32,34]. Within animals, this correlation was not reliable (-0.12 ± 0.05, mean ± s.e.m., $P > 0.05$ in 6 out of 8 animals), despite widespread sampling (Supplementary Fig. 19). However, the ITF was more similar for grid cells from the same module than grid cells from different modules (Fig. 6b, c). In 7 out of 8 animals, the ITF was more similar for cell pairs with similar grid scale (<5th percentile of all pairwise differences in grid scale) than for pairs with different scale (>5th percentile) (Fig. 6c; ratio of 1.33 ± 0.08, mean ± s.e.m., $t(7) = 4.37$, $P < 0.005$, Student's t-test). This comodularity was not caused by any relationship between grid theta frequency and grid spacing, as the residuals of the linear regression between ITF and grid spacing remained more similar for cell pairs with similar grid scale (7 of 8 animals, ratio of 1.26 ± 0.10, $t(7) = 2.59$, $P < 0.05$). Taken together, these observations show that modules of grid cells with similar geometric properties are discrete also with regard to temporal organization, and that this temporal organization does not exhibit any strong linear or monotonic relationship to grid spacing.

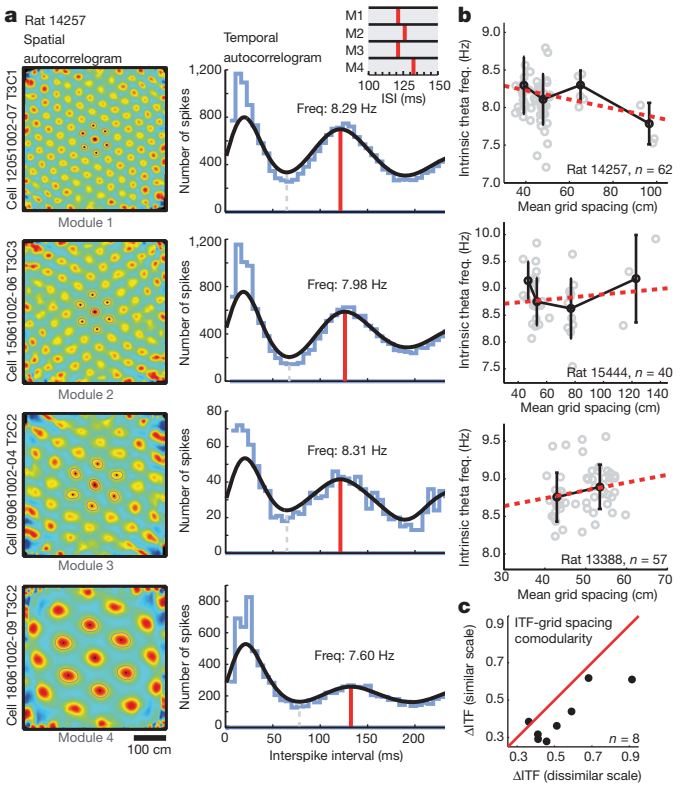

Figure 6 | Comodularity between grid spacing and theta frequency. **a**, Theta modulation in four cells from four grid modules in rat 14527. Left, spatial autocorrelograms. Right, spike-time autocorrelograms for the same cells. Peaks (red line) in the theta range were used to calculate each grid cell's intrinsic theta frequency (ITF, indicated above each peak). Top inset, close-up of peak interspike interval (ISI) for each module. **b**, ITF as a function of grid spacing in three animals. Circles indicate cells. Mean and s.d. of ITF are shown for each module. Red dashed lines indicate best linear fits. Note modular appearance of the theta modulation as well as lack of linear or monotonic relationship between grid spacing and theta modulation. **c**, Comparison of average differences in ITF for pairs of grid cells with similar grid spacing (<5th percentile of scale differences) and pairs with different spacing (>5th percentile) (all animals, methods as in Fig. 2d).

Functional independence of grid modules

We have found that grid scale, grid orientation and grid distortion, as well as temporal organization in the theta frequency range, are determined independently for different modules of the same grid network. To address directly the question of whether the modules are also decoupled in their responses to changes in the environment, we tested four animals in an environmental compression task known to induce temporary rescaling in grid cells[30].

Grid cells from different modules were first recorded in a familiar 150 cm × 150 cm environment, then in a novel 150 cm × 100 cm version of the same environment, and then again in the original environment (Fig. 7a–c). To quantify any rescaling in the compressed environment, we stretched each rectangular rate map iteratively in small increments and correlated, for each step, the stretched map with the overlapping region of the cell's square map. This yielded

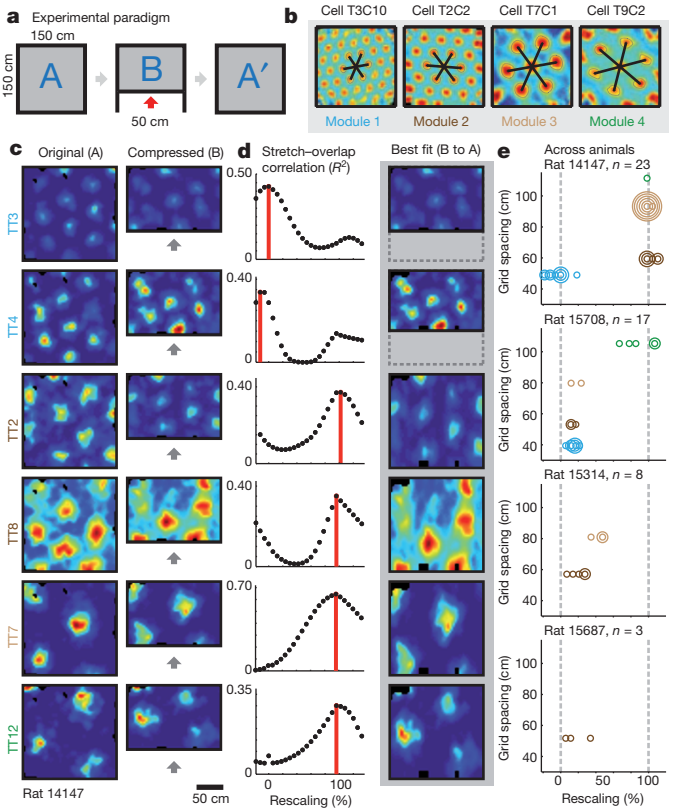

Figure 7 | Grid modules are functionally independent. **a**, Schematic of the box-compression experiment. **b**, Spatial autocorrelograms from individual cells representing 4 modules in rat 14147. **c**, Rate maps from 6 grids on 6 different tetrodes in the box-compression task (rat 14147). Tetrode numbering is arbitrary. Only configurations A and B are shown. Wall relocation indicated by grey arrows. **d**, Left, stretch-correlation curves showing spatial correlation between the rate map in B and the overlapping part of A for successive expansions of the map in B. Peak values are indicated by red lines. Best fits are shown to the right. Note distinct responses of grids in module M1 (TT3, TT4) as compared to grids in M2–M4 (remaining tetrodes, all with larger grid spacing). **e**, Rescaling as a function of module scale. Circles correspond to individual cells. Concentric rings represent overlapping data points. For clarity, individual grids are represented by the mean grid spacing of the respective module. Colour code as in **b**.

stretch-correlation curves from which we could define each cell's rescaling level as the amount of stretch that gave rise to the largest correlation (Fig. 7d). The degree of rescaling varied substantially (from −18 to 110%; mean ± s.e.m. = 35.1 ± 17.0%; 4 animals, 51 grid cells). Within individual rats, the distribution of rescaling values was generally bimodal, with clusters forming near 0% and 100% (Fig. 7e and Supplementary Fig. 20); cells either rescaled fully with the environment or did not rescale at all.

The key finding is that simultaneously recorded grid modules responded independently to the relocation of the wall (Fig. 7c–e and Supplementary Fig. 20). Grid cells in Module M1, with the smallest grid-scale values, showed only minimal rescaling, with peak correlations appearing between −18.4% and 21.4% of the stretch distance. At the same time, grid cells in the larger modules rescaled completely, such that all fields of the original environment were maintained, but with reduced grid-field distances in the compressed direction. Cells that belonged to the same module always responded coherently (Fig. 7c–e). Taken together, these data provide proof-of-principle evidence that grid modules can operate independently on geometric inputs from the same environment.

Discussion

Our understanding of population dynamics in the entorhinal grid network has lagged behind that of individual grid cells for the very reason that, until now, experimenters have not been able to collect data from more than a dozen grid cells in the same animal[18–20,30–38]. By increasing this number by an order of magnitude, and by recording from multiple locations within the same MEC circuit at the same time, we were able to obtain sufficiently dense cell sampling to show that the grid-cell population is discretized into functionally independent subpopulations. Whereas the scale of the grid map was found to increase topographically from dorsal to ventral MEC when the data were pooled across animals, as in previous work[19,20,30,36], there was no corresponding smoothness in individual animals. In every single animal, the progression of grid scale was step-like. Because step sizes and step ratios were unique for each animal, the discrete nature of the distribution is masked in the pooled data. Our study further showed that more than one grid orientation can be expressed simultaneously in the same animal[37], and that discontinuities in grid orientation coincide with discontinuities in grid scale. The presence of only a single grid orientation in previous work[38] probably reflects limited sampling. Finally, cell populations with different grid properties were found to respond independently to changes in the geometry of the environment, indicating that modules of grid cells can be anchored separately to external cues or boundaries. The discrete but interspersed topography of the grid map, and the apparent autonomy of the modules, differs from the graded topography of maps for continuous variables in well-studied sensory systems, such as the orientation and direction maps of the feline, weasel and primate visual cortex[4–11].

The cellular substrate of the grid modules remains to be determined. The MEC has several architectonic features that might favour modular operations[29], such as the organization of entorhinal neurons into a mosaic of alternating cytochrome-oxidase-rich and cytochrome-oxidase-poor clusters[39,40] or the segregation of cell groups by bundles of axons and dendrites from cells in the intermediate and deep layers[41]. However, none of these, or other known structural variations[29], match the anatomical distribution of grid modules. First, the number of MEC clusters formed by bundling or variations in cytochrome oxidase expression is probably in the order of hundreds, whereas the number of grid-cell modules, identified within a range that covered up to 50% of the dorsoventral axis of the MEC, on the medial side, never exceeded 4 or 5. Second, the horizontal band-like appearance of the grid modules, with detectable clustering in the dorsoventral but not the mediolateral dimension, is inconsistent with the patchy patterns observed in the anatomical stains. Finally, grid modules exhibit considerable anatomical overlap, cutting across cell layers as well as widespread regions along both axes of the MEC sheet. The data indicate that grid modules are partly entangled and raise the possibility that, within the same anatomical space, there are multiple cell groups with strong internal connectivity and weak cross-connectivity. How overlapping networks are segregated remains to be determined, but the invariance of the average scale ratio, across animals and successive modules, implies a genetic mechanism, possibly one in which the formation of modules is determined by self-organizing cortical mechanisms during cortical development[21], at the same time as the variability in actual values for grid spacing across animals retains a role for experience in calibrating the grid modules to the external environment. The emergence of grid patterns from local inhibitory coupling[26,42], and the absence of precise spatial periodicity before the maturation of such coupling[43,44], point to inhibitory networks as a possible component of the mechanism for developmental segregation of grid modules.

The modular nature of the grid-cell network has implications for the mechanisms of grid formation. Computational models of grid cells fall into two main classes—oscillatory interference models and attractor–network models[17,22]. Both types of models make predictions relevant to the functional organization of the grid-cell network. The interference models suggest that grid patterns emerge from velocity-dependent beat frequencies in the membrane potential formed by interference between multiple theta oscillators at slightly different frequencies[24,45,46]. Following this idea, increases in grid scale must be paralleled by proportional decreases in the cells' theta modulation frequency. The lack of such a linear relationship across modules does not support a theta frequency-based mechanism for grid cells and reinforces the recent observation that grid cells persist in the absence of theta rhythmicity[36]. In the second class of models—the attractor models—the changing location of a moving animal is represented instead by translation of activity across an array of grid cells arranged in network space according to their grid phase, with direction and distance of displacement in this array being proportional to the actual movement of the animal in the environment[21,23,26,42]. This proposed correspondence between velocity of movement and displacement in the neural sheet can only be maintained if the local network has a common grid scale and grid orientation, that is if the network is organized into discrete space and orientation modules. The present work confirms this prediction. By showing that grid modules with different spacing and orientation can interact independently with the environment, the present study further raises the possibility that the MEC comprises multiple path-integrating grid networks, each operating at a unique grid scale, possibly as the result of a unique amplification of incoming speed signals[21].

The modular organization of grid cells may further influence how information is processed and stored downstream in the hippocampus. If hippocampal place cells are excited by convergent input from multiple grid modules, two types of effects can be envisaged. First, convergence of signals from multiple grid modules would prevent propagation of noise that is uncorrelated across modules, allowing the hippocampus to estimate location with a precision that exceeds that of the individual grid modules[26,47]. Second, such convergence might facilitate the formation of new and unique representations for new environments. If converging modules respond independently to displacement or reconfiguration of the environment, the altered co-activity may activate a new subset of hippocampal neurons at each location in the changed environment[35]. A similarly effective redistribution would not necessarily be seen if the entire grid map responded coherently. Computational simulations have shown that convergence of signals from only 2 to 4 independently aligned grid modules may be sufficient to obtain near-complete remapping in downstream place cells[48]. Each change in relative phase and orientation among a set of grid modules might lead to a unique hippocampal activation pattern, suggesting that the number of distinct representations that can be formed is large[49,50]. By combining input from a small number of independently operating grid modules, hippocampal cell

populations may thus acquire the ability to generate discrete representations individualized to specific places and experiences, an ability that may lie at the heart of the contribution of the hippocampus to episodic and semantic memory formation.

METHODS SUMMARY

Male Long-Evans rats were implanted with a microdrive carrying a single bundle of 4 tetrodes angled tangentially to the MEC surface (5 rats) or with a 'hyperdrive' carrying 12 independently movable tetrodes targeted semi-vertically to widespread regions of the MEC (10 rats). The tetrodes were advanced in small increments over weeks until large numbers of stable grid cells appeared. Neural activity was recorded while the rats foraged in 100–220-cm-wide open-field boxes. Cells were assigned to modules using a *k*-means clustering algorithm. A complete description of the materials and methods is provided in Supplementary Information.

Received 16 May; accepted 28 September 2012.

1. Mountcastle, V. B. Modality and topographic properties of single neurons of cat's somatic sensory cortex. *J. Neurophysiol.* **20,** 408–434 (1957).
2. Hubel, D. H. & Wiesel, T. Receptive fields, binocular interaction, and functional architecture of cat striate cortex. *J. Physiol. (Lond.)* **160,** 106–154 (1962).
3. Hubel, D. H. & Wiesel, T. Functional architecture of macaque monkey visual cortex. *Proc. R. Soc. Lond. B Biol. Sci.* **198,** 1–59 (1977).
4. Hubel, D. H. & Wiesel, T. Sequence regularity and geometry of orientation columns in the monkey striate cortex. *J. Comp. Neurol.* **158,** 267–293 (1974).
5. Blasdel, G. G. & Salama, G. Voltage sensitive dyes reveal a modular organization in monkey striate cortex. *Nature* **321,** 579–585 (1986).
6. Bonhoeffer, T. & Grinvald, A. Orientation columns in cat are organized in pin-wheel like patterns. *Nature* **353,** 429–431 (1991).
7. Ohki, K. *et al.* Highly ordered arrangement of single neurons in orientation pinwheels. *Nature* **442,** 925–928 (2006).
8. Payne, B. R., Berman, N. & Murphy, E. H. Organization of direction preferences in cat visual cortex. *Brain Res.* **211,** 445–450 (1981).
9. Tolhurst, D. J., Dean, A. F. & Thompson, I. D. Preferred direction of movement as an element in the organization of cat visual cortex. *Exp. Brain Res.* **44,** 340–342 (1981).
10. Weliky, M., Bosking, W. H. & Fitzpatrick, D. A systematic map of direction preference in primary visual cortex. *Nature* **379,** 725–728 (1996).
11. Ohki, K., Chung, S., Ch'ng, Y. H., Kara, P. & Reid, R. C. Functional imaging with cellular resolution reveals precise micro-architecture in visual cortex. *Nature* **433,** 597–603 (2005).
12. Sperry, R. W. Visuomotor coordination in the newt (*Triturus viridescens*) after regeneration of the optic nerve. *J. Comp. Neurol.* **79,** 33–55 (1943).
13. Drescher, U. *et al. In vitro* guidance of retinal ganglion cell axons by RAGS, a 25 kDa tectal protein related to ligands for Eph receptor tyrosine kinases. *Cell* **82,** 359–370 (1995).
14. Cheng, H. J., Nakamoto, M., Bergemann, A. D. & Flanagan, J. G. Complementary gradients in expression and binding of ELF-1 and Mek4 in development of the topographic retinotectal projection map. *Cell* **82,** 371–381 (1995).
15. O'Keefe, J. & Dostrovsky, J. The hippocampus as a spatial map. Preliminary evidence from unit activity in the freely-moving rat. *Brain Res.* **34,** 171–175 (1971).
16. O'Keefe, J. & Nadel, L. *The Hippocampus as a Cognitive Map* (Oxford Univ. Press, 1978).
17. Moser, E. I., Kropff, E. & Moser, M.-B. Place cells, grid cells, and the brain's spatial representation system. *Annu. Rev. Neurosci.* **31,** 69–89 (2008).
18. Fyhn, M., Molden, S., Witter, M. P., Moser, E. I. & Moser, M. B. Spatial representation in the entorhinal cortex. *Science* **305,** 1258–1264 (2004).
19. Hafting, T., Fyhn, M., Molden, S., Moser, M.-B. & Moser, E. I. Microstructure of a spatial map in the entorhinal cortex. *Nature* **436,** 801–806 (2005).
20. Sargolini, F. *et al.* Conjunctive representation of position, direction, and velocity in entorhinal cortex. *Science* **312,** 758–762 (2006).
21. McNaughton, B. L., Battaglia, F. P., Jensen, O., Moser, E. I. & Moser, M.-B. Path integration and the neural basis of the 'cognitive map'. *Nature Rev. Neurosci.* **7,** 663–678 (2006).
22. Giocomo, L. M., Moser, M.-B. & Moser, E. W. I. Computational models of grid cells. *Neuron* **71,** 589–603 (2011).
23. Fuhs, M. C. & Touretzky, D. S. A spin glass model of path integration in rat medial entorhinal cortex. *J. Neurosci.* **26,** 4266–4276 (2006).
24. Burgess, N., Barry, C. & O'Keefe, J. An oscillatory interference model of grid cell firing. *Hippocampus* **17,** 801–812 (2007).
25. Kropff, E. & Treves, A. The emergence of grid cells: intelligent design or just adaptation? *Hippocampus* **18,** 1256–1269 (2008).
26. Burak, Y. & Fiete, I. R. Accurate path integration in continuous attractor network models of grid cells. *PLOS Comput. Biol.* **5,** e1000291 (2009).
27. Zilli, E. A. & Hasselmo, M. E. Coupled noisy spiking neurons as velocity-controlled oscillators in a model of grid cell spatial firing. *J. Neurosci.* **30,** 13850–13860 (2010).
28. Mhatre, H., Gorchetchnikov, A. & Grossberg, S. Grid cell hexagonal patterns formed by fast self-organized learning within entorhinal cortex. *Hippocampus* **22,** 320–334 (2012).
29. Witter, M. P. & Moser, E. I. Spatial representation and the architecture of the entorhinal cortex. *Trends Neurosci.* **29,** 671–678 (2006).
30. Barry, C., Hayman, R., Burgess, N. & Jeffery, K. J. Experience-dependent rescaling of entorhinal grids. *Nature Neurosci.* **10,** 682–684 (2007).
31. Solstad, T., Boccara, C. N., Kropff, E., Moser, M.-B. & Moser, E. I. Representation of geometric borders in the entorhinal cortex. *Science* **322,** 1865–1868 (2008).
32. Brun, V. H. *et al.* Progressive increase in grid scale from dorsal to ventral medial entorhinal cortex. *Hippocampus* **18,** 1200–1212 (2008).
33. Hafting, T., Fyhn, M., Bonnevie, T., Moser, M.-B. & Moser, E. I. Hippocampus-independent phase precession in entorhinal grid cells. *Nature* **453,** 1248–1252 (2008).
34. Jeewajee, A., Barry, C., O'Keefe, J. & Burgess, N. Grid cells and theta as oscillatory interference: electrophysiological data from freely moving rats. *Hippocampus* **18,** 1175–1185 (2008).
35. Fyhn, M., Hafting, T., Treves, A., Moser, M. B. & Moser, E. I. Hippocampal remapping and grid realignment in entorhinal cortex. *Nature* **446,** 190–194 (2007).
36. Yartsev, M. M., Witter, M. P. & Ulanovsky, N. Grid cells without theta oscillations in the entorhinal cortex of bats. *Nature* **479,** 103–107 (2011).
37. Krupic, J., Burgess, N. & O'Keefe, J. Neural representations of location composed of spatially periodic bands. *Science* **337,** 853–857 (2012).
38. Doeller, C. F., Barry, C. & Burgess, N. Evidence for grid cells in a human memory network. *Nature* **463,** 657–661 (2010).
39. Hevner, R. F. & Wong-Riley, M. T. Entorhinal cortex of the human, monkey, and rat: metabolic map as revealed by cytochrome oxidase. *J. Comp. Neurol.* **326,** 451–469 (1992).
40. Burgalossi, A. *et al.* Microcircuits of functionally identified neurons in the rat medial entorhinal cortex. *Neuron* **70,** 773–786 (2011).
41. Ikeda, J., Mori, K., Oka, S. & Watanbe, Y. A columnar arrangement of dendritic processes of entorhinal cortex neurons revealed by a monoclonal antibody. *Brain Res.* **505,** 176–179 (1989).
42. Couey J. J. *et al.* Medical entorhinal cortex layer ii stellate cells are embedded within a recurrent inhibitory network. *Soc. Necuosci. abstr.* 702.06 (2012).
43. Langston, R. F. *et al.* Development of the spatial representation system in the rat. *Science* **328,** 1576–1580 (2010).
44. Wills, T. J., Cacucci, F., Burgess, N. & O'Keefe, J. Development of the hippocampal cognitive map in preweanling rats. *Science* **328,** 1573–1576 (2010).
45. Hasselmo, M. E., Giocomo, L. M. & Zilli, E. A. Grid cell firing may arise from interference of theta frequency membrane potential oscillations in single neurons. *Hippocampus* **17,** 1252–1271 (2007).
46. Blair, H. T., Welday, A. C. & Zhang, K. Scale-invariant memory representations emerge from moiré interference between grid fields that produce theta oscillations: a computational model. *J. Neurosci.* **27,** 3211–3229 (2007).
47. Sreenivasan, S. & Fiete, I. Grid cells generate an analog error-correcting code for singularly precise neural computation. *Nature Neurosci.* **14,** 1330–1337 (2011).
48. Monaco, J. D. & Abbott, L. F. Modular realignment of entorhinal grid cell activity as a basis for hippocampal remapping. *J. Neurosci.* **31,** 9414–9425 (2011).
49. Muller, R. U. & Kubie, J. L. The effects of changes in the environment on the spatial firing of hippocampal complex-spike cells. *J. Neurosci.* **7,** 1951–1968 (1987).
50. Colgin, L. L., Moser, E. I. & Moser, M.-B. Understanding memory through hippocampal remapping. *Trends Neurosci.* **31,** 469–477 (2008).

Supplementary Information is available in the online version of the paper.

Acknowledgements We thank A. M. Amundgård, K. Haugen, K. Jenssen, E. Kråkvik, R. Skjerpeng, and H. Waade for technical assistance, J. Whitlock for implanting an animal in the tangential group, and T. Bonhoeffer, B. Dunn, B. McNaughton, Y. Roudi, A. Treves and A. Witoelar for helpful discussion. The work was supported by an Advanced Investigator Grant from the European Research Council ('CIRCUIT', Grant Agreement no. 232608), the Kavli Foundation and the Centre of Excellence scheme of the Research Council of Norway.

Author Contributions T.St., H.S., T.So., M.-B.M. and E.I.M. designed experiments and analyses; H.S., T.St. and T.So. implanted tetrodes; H.S. recorded multisite data; T.So. and K.F. tested animals with tangential implants; T.St. performed the majority of the analyses; and T.St. and E.I.M. wrote the paper with input from all authors.

Author Information Reprints and permissions information is available at www.nature.com/reprints. The authors declare no competing financial interests. Readers are welcome to comment on the online version of the paper. Correspondence and requests for materials should be addressed to E.I.M. (edvard.moser@ntnu.no) or H.S. (hanne.stensola@ntnu.no) or T.St. (tor.stensola@ntnu.no).